JOURNAL OF GEOPHYSICAL RESEARCH, VOL. 114, C01018, doi:10.1029/2008JC004998, 2009

On wind-wave-current interactions during the Shoaling Waves Experiment

Fei W. Zhang,[1] William M. Drennan,[1] Brian K. Haus,[1] and Hans C. Graber[1]

Received 30 June 2008; revised 29 September 2008; accepted 17 November 2008; published 30 January 2009.

[1] This paper presents a case study of wind-wave-current interaction during the Shoaling Waves Experiment (SHOWEX). Surface current fields off Duck, North Carolina, were measured by a high-frequency Ocean Surface Current Radar (OSCR). Wind, wind stress, and directional wave data were obtained from several Air Sea Interaction Spar (ASIS) buoys moored in the OSCR scanning domain. At several times during the experiment, significant coastal currents entered the experimental area. High horizontal shears at the current edge resulted in the waves at the peak of wind-sea spectra (but not those in the higher-frequency equilibrium range) being shifted away from the mean wind direction. This led to a significant turning of the wind stress vector away from the mean wind direction. The interactions presented here have important applications in radar remote sensing and are discussed in the context of recent radar imaging models of the ocean surface.

Citation: Zhang, F. W., W. M. Drennan, B. K. Haus, and H. C. Graber (2009), On wind-wave-current interactions during the Shoaling Waves Experiment, *J. Geophys. Res.*, *114*, C01018, doi:10.1029/2008JC004998.

1. Introduction

[2] The surface wind stress, or air-sea flux of momentum, is one of the key input parameters for atmospheric, oceanic circulation, and wave models. For example, it drives the growth of surface gravity waves and controls the degree of wave breaking and thence near surface mixing. Understanding and quantifying wind stress is important for meteorologists, oceanographers, and climatologists. While numerous studies have investigated the magnitude of the wind stress vector [e.g., *Smith*, 1980; *Large and Pond*, 1981], our focus here is on the direction of the stress vector, more specifically on deviations of the stress direction from that of the wind.

[3] The wind stress vector $\hat{\tau}$ is given by

$$\hat{\tau} = \rho\{(-\overline{u'w'})\hat{i} + (-\overline{v'w'})\hat{j}\} \tag{1}$$

where ρ is the air density, and $\hat{i}$ and $\hat{j}$ represent the longitudinal (downwind) and lateral (off-wind) unit vectors. The fluctuating velocity components u', v', and w', in the mean downwind, off-wind, and vertical directions, respectively, are derived from the instantaneous velocities by the Reynolds decomposition method. The overbar represents time averages over periods of order 20 min. We define the direction of the wind stress with respect to the mean wind, θ, as

$$\tan\theta = (-\overline{v'w'})/(-\overline{u'w'}). \tag{2}$$

Here positive angles correspond to the stress vector oriented to the right of the wind vector. In a similar fashion, the current velocity can be written as $\hat{U}_c = (U_{cX})\hat{i} + (U_{cY})\hat{j}$ where U_{cX} and U_{cY} are the components in the downwind and off-wind directions. The off-wind current direction is given by $\tan\theta_c = U_{cY}/U_{cX}$.

[4] In many early studies [e.g., *Busch*, 1977; *Large and Pond*, 1981], the off-wind stress $(-\overline{v'w'})$ was either ignored or assumed to be insignificant with respect to the $(-\overline{u'w'})$ term. This is consistent with Monin-Obukhov (MO) similarity theory [*Monin and Obukhov*, 1954], which assumes that the stress vector is aligned with the wind vector. It is also consistent with measurements over land. In the absence of buoyancy, MO theory predicts the stress to be related solely to the relative wind speed $U_Z - U_0$, where U_Z is the mean wind speed at reference height z, $U_0 = |\hat{U}_c|$ and U_{cY} is assumed small (so $U_0 \approx U_{cX}$ is in the along wind direction):

$$|\hat{\tau}| \approx \rho(-\overline{u'w'}) = \rho C_{Dz}(U_z - U_0)^2. \tag{3}$$

Here C_{Dz} is the z meter drag coefficient.

[5] However, over 15% of *Smith*'s [1980] stress data over the sea were found to have relative stress directions $|\theta| > 26°$. Many other data sets show similar results. See for instance Figure 1 showing wind speed and stress angle relative to the wind direction during the SHOWEX experiment, which is discussed below. Note in particular days 307 and 308, when the wind stress veered as much as 50° off the mean wind direction. While not advocating the practice is general, Smith eliminated these cases from his data set due to uncertainties over possible contamination due to sensor motion.

[6] More recently however, such data have been retained, and efforts have been made to understand the physics behind the development of off-wind stress components. *Zemba and Friehe* [1987], in their aircraft study of a California coastal jet, observed the off-wind stress angle

[1]Rosenstiel School for Marine and Atmospheric Science, University of Miami, Miami, Florida, USA.

0148-0227/09/2008JC004998$09.00

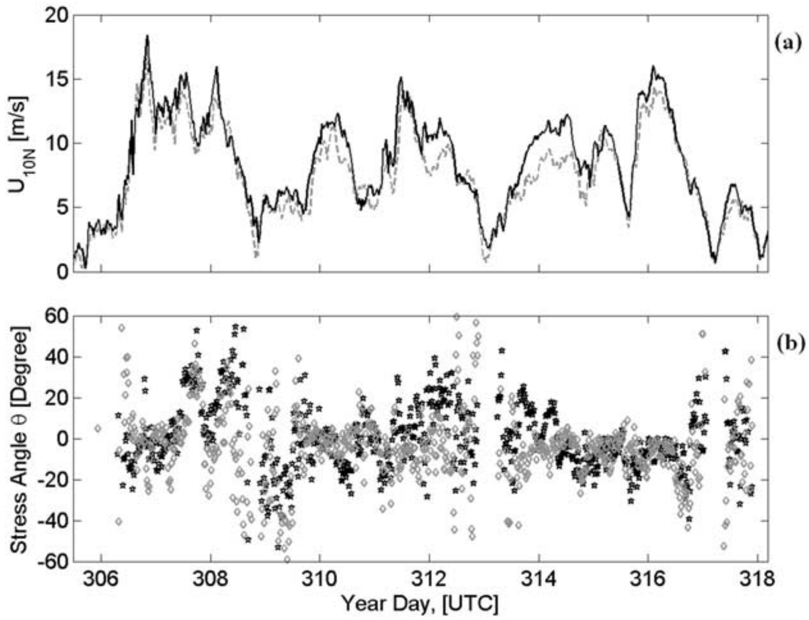

Figure 1. (a) Wind speed and (b) wind stress angle with respect to the wind during the SHOWEX experiment of 1999. Dashed and solid lines in Figure 1a show data from the Bravo and Yankee buoys, respectively. In Figure 1b, Bravo data are indicated by stars and Yankee data are indicated by diamonds. Wind stress angles are shown only for wind speeds over 4 m s^{-1}.

to increase with height from near zero 30 m above the surface to almost 60° at 170 m. They attributed the shift to Eckman turning of the coastal wind jet.

[7] For many years now [e.g., *Kitaigorodskii*, 1973], surface gravity waves have been known to affect surface stress (and vice versa). While the earlier studies focused on the wind stress magnitude, more recent work has investigated the effect of waves on the stress angle. *Geernaert et al.* [1993], with simultaneous field measurements of both the wind stress vector and the directional wavefield, showed a qualitative relationship between wind stress angle and angle of swell waves (both with respect to the wind). Similar results were found by *Rieder et al.* [1994] and *Grachev et al.* [2003].

[8] The effect of surface currents on wind stress direction has been given less attention. A current colinear with the wind is expected to influence the stress only through its effect on the relative wind speed. Over much of the open ocean, surface currents are largely wind driven, with a magnitude of order 3% of mean wind speed [*Wu*, 1975]. In these cases the effect of currents on stress is small and usually neglected. However, near the equator surface currents are of order 1 m s^{-1}, compared to surface winds around 6 m s^{-1}. Western boundary currents (e.g., the Gulf Stream) may approach 2 m s^{-1} [*Richardson and McKee*, 1984; *Weisberg*, 1984]. Buoyancy and tidal currents are also significant in some coastal regions. In these conditions, the neglect of surface current in the bulk relation (3) can modify the wind stress by O(20%).

[9] *Cornillon and Park* [2001], *Dickinson et al.* [2001], *Kelly et al.* [2001, 2005], and *Polito et al.* [2001] studied the effects of ocean currents on the accuracy of scatterometer winds. They found differences in both magnitude and direction of scatterometer winds and in situ wind measurements, which were attributed in part to surface currents. *Drennan and Shay* [2006], with in situ measurements of wind, wind stress, and surface currents, reported a steering of the stress away from the mean wind direction by almost 30°, which they attributed to strong off-wind currents. *Haus* [2007] demonstrated that off-wind current shear led to reduced wave growth rates, which could be explained by stress veering.

[10] In this study, we investigate the effect of currents on wind stress, through their effect on the wavefield. This paper expands our understanding from previous work using a comprehensive data set from buoys and coastal radar collected during the 1999 Shoaling Waves experiment (SHOWEX). We first introduce the experiment (section 2), and then describe the effect of horizontally sheared currents on the wind stress (section 3). In section 4, we will discuss the observed phenomena in the context of present theories. The conclusion of the article will be presented in section 5.

2. Shoaling Waves Experiment

[11] SHOWEX took place off Duck, North Carolina, during October–December 1999. The goal of this experiment was to study the properties and evolution of surface gravity waves in intermediate depths and shallow water. The experimental domain (Figure 2) is interesting for air-sea interaction research as it is influenced by several distinct sources of forcing: the Chesapeake Bay buoyancy current [*Rennie et al.*, 1999; *Haus et al.*, 2004]; the Gulf Stream; swell waves propagating onshore; and winds from a variety of directions. In order to consider all of above parameters, the SHOWEX experiment was designed as a comprehensive research project which involved aircraft, research vessels, buoys, high-frequency (HF) radar, and satellites. The focus

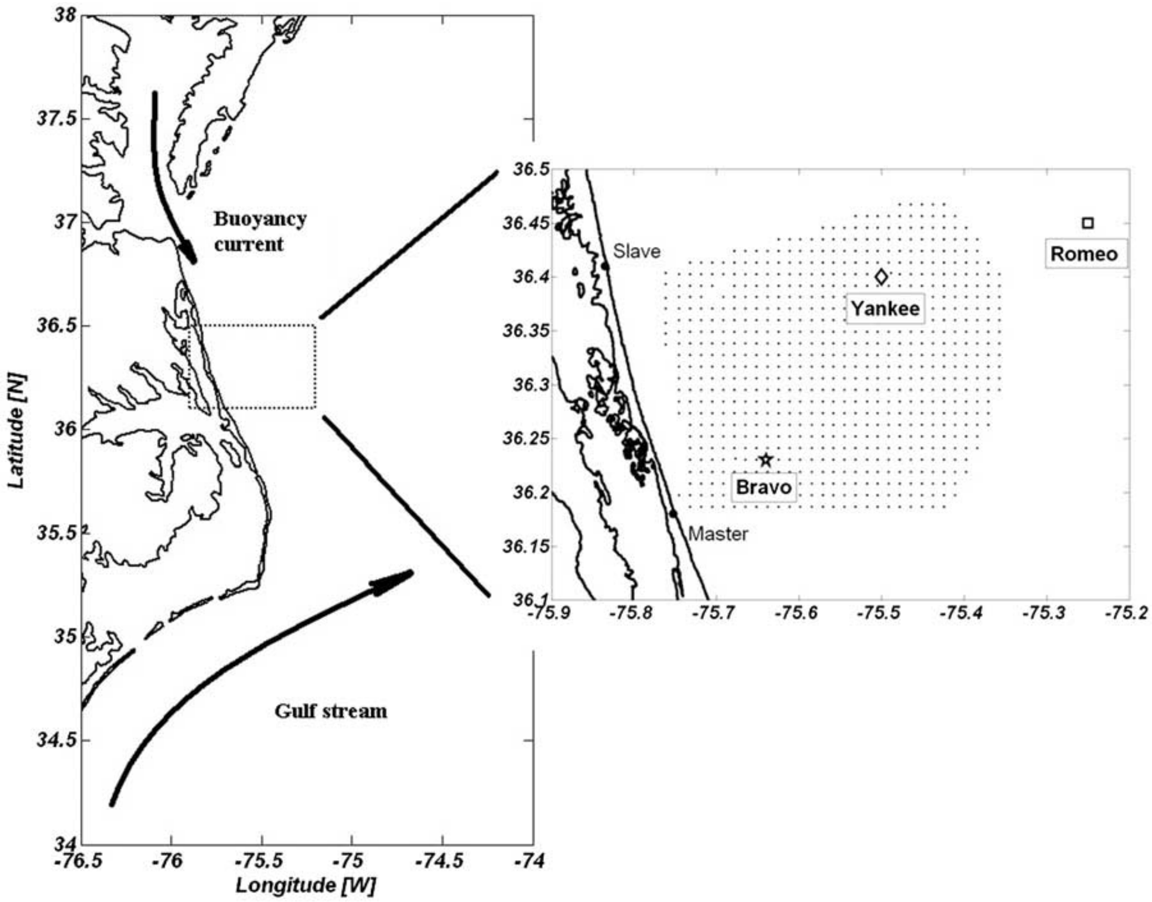

Figure 2. Location of the Shoaling Waves Experiment near Duck, North Carolina, showing the OSCR antenna sites (large dots) and cells (small dots), and ASIS buoys (Bravo is shown by a star; Yankee is shown by a diamond; Romeo is shown by a square). Significant currents are also shown.

of the present study is the evolution of the wavefield in the presence of inhomogeneous surface currents and on how the resulting wavefield affects the wind stress direction. Surface current fields from the HF radar, along with directional wave spectra and direct air-sea fluxes from buoys moored within the radar footprint will be used.

2.1. Ocean Surface Current Radar

[12] During SHOWEX, the University of Miami Ocean Surface Current Radar (OSCR) system was deployed starting on 27 October 1999 (Year Day 300) and ending on 10 December (YD 344). OSCR consisted of two HF radar transmit/receive stations. One station was located at the U.S. Army Corps of Engineers Field Research Facility, 36°11′N, 75°49′W and the other was at 25 km to the north at 36°25′N, 75°50′W (Figure 2). OSCR was operated at a frequency of 25.4 MHz, which resulted in a transmitted radar wavelength of 11.8 m and a Bragg scattering ocean wavelength of 5.9 m [*Stewart and Joy*, 1974]. At this frequency, the OSCR data represent the average current over the top 1 m depth. With a signal dwell time of 5 min, the radar velocity accuracy was 0.02 m s^{-1} [*Prandle*, 1987]. OSCR observed the surface current at 700 cells over a 1200 km^2 sampling area (see Figure 2) with a spatial resolution of 1 km^2. Further details on the OSCR deployment in SHOWEX can be found in the work of *Wyatt et al.* [2005]. Note that OSCR did not collect useful information from YD 319 to 324 due to disk failure resulting from a power surge.

2.2. Air-Sea Interaction Spar (ASIS) Buoys

[13] Three ASIS buoys [*Graber et al.*, 2000] were deployed in a roughly shore-normal line (Figure 2) to measure the evolution of surface waves, the air-sea turbulent fluxes of momentum and buoyancy and mean meteorology over the shelf. Two of the buoys, Bravo and Yankee, were moored in the scanning area of OSCR. The third buoy, Romeo, was deployed further offshore, outside of the OSCR domain. Since this paper considers the current and wind stress together, only data from Bravo and Yankee are used in the analysis. Bravo was deployed on YD 302 at 36°14′N, 75°40′W at a depth of 20 m. Yankee was deployed the next day at 36°25′N, 75°31′W in 30 m. Bravo operated continuously until late on YD 326 when the anemometer failed due to power limitations. Yankee, with extra batteries, operated continuously until recovery on YD 347.

[14] Although each of the buoys was configured with somewhat different sensor suites, the instruments of most interest here were identical. The wind vector was measured with three-axis sonic anemometers (Gill Solent 1012R2A) at 7 m above the mean surface. From the sonic anemometer signals, the three orthogonal components of the wind, along with speed of sound c, were recorded. A motion package,

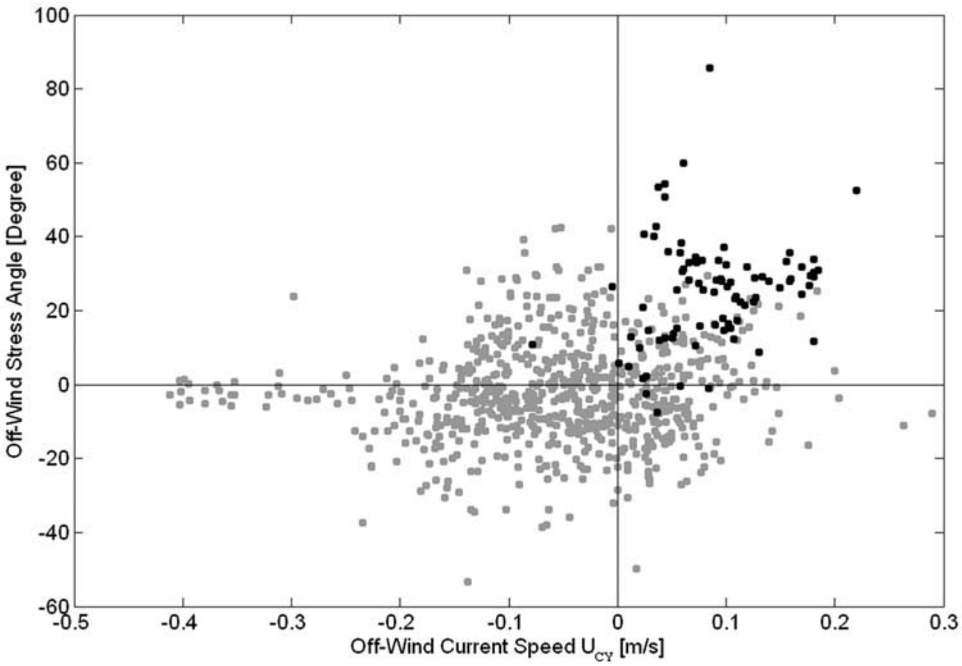

Figure 3. Off-wind stress angle plotted against the off-wind current speed from Bravo during YD 306–318. Only data for wind speeds above 4 m s^{-1} are shown. The black data are from the period of interest (POI) identified in the text.

consisting of three orthogonal pairs of rate gyros (Systron Donner GC1-00050-100) and linear accelerometers (Columbia Research Laboratory SA-307HPTX) and a compass (Precision Navigation TCM-2), was installed in an underwater housing on each buoy. These motion data were used to correct the measured wind components to a stationary frame based on an algorithm given by *Anctil et al.* [1994] and *Drennan et al.* [2003]. The motion corrected velocity data were rotated into the mean wind direction (i.e., $\overline{v}$ = 0); an average tilt correction is used to force $\overline{w}$ = 0. Mean air temperature and relative humidity were measured at 4 m with Rotronic MP-100C sensors. As the Rotronic on Bravo failed, air temperature and humidity data from Yankee are used instead. Current magnitudes and bulk water temperature were measured at 10 m depth using Sensor-Tek UCM-60DL current meters. Bravo was equipped with an additional thermistor (Brancker XL) at 5 m depth. Currents at the surface (OSCR) and 10 m depth show good agreement in the majority of cases (not shown). The differences between the two measurements can be mainly attributed to the depth difference [*Graber et al.*, 1997].

[15] All signals (excepting the UCM and Brancker) were sampled at 20 Hz for 60-min periods, and the data were processed in blocks of 20 min. Data collected when the wind was blowing through the back of the sonic anemometer were eliminated. This eliminated about 10% of the runs, typically those where the wind forcing is too low to keep ASIS pointed into the wind. After motion and tilt corrections, the velocity signals were detrended prior to calculation of the stress vector components. The sonic temperature $t_s = (c/20.067)^2$ was corrected for off-wind contamination [*Kaimal and Gaynor*, 1991] and used to calculate the buoyancy flux $\overline{t_s'w'}$. As described by *Drennan and Shay* [2006], the Obukhov length L is then calculated from the measured buoyancy and momentum fluxes: $L = -u_*^3\ \Theta_v\ [\kappa\ g\ \overline{t_s'w'}]^{-1}$. Here $u_* = [|\tau|/\rho]^{1/2}$ is the friction velocity, Θ_v is the mean virtual temperature, κ = 0.4 is the von Kármán constant, and g is the gravitational constant. Finally, 10 m neutrally stratified wind speeds were calculated using the profile functions Ψ of *Donelan* [1990]: $U_z - U_0 = (u_*/\kappa)\ [\log(z/z_o) - \Psi(z/L)]$, where z_o is the surface roughness length.

[16] Each ASIS was equipped with an eight-element array of 3.5 m long × 0.9 mm diameter capacitance wave gauges (a centered pentagon of 0.93 m radius with three gauges in the center). The wave array data were corrected for the motion of the buoy [*Drennan et al.*, 1994; *Pettersson et al.*, 2003]. The maximum likelihood method was then applied to obtain directional wave spectra [*Capon*, 1969]. The wind sea component was defined using the criteria $U_{10N}\cos(\theta_d) > 0.83C_p$ [*Donelan et al.*, 1985], and $\theta_d < 45°$, where θ_d is the angle between the mean wind and waves and C_p the phase speed at the spectral peak. Other components were identified as swell waves.

3. Data Analysis

[17] The data from both Bravo and Yankee during the period YD 305–318, when both buoys and the radar were functioning, were chosen for in-depth analysis. As noted previously, there are several occasions during this time when the wind stress direction was significantly different from that of the mean wind (Figure 1). As pointed out above, many different mechanisms have been associated with off-wind stress angles. These include off-wind surface currents, turning winds, and swell waves propagating from off-wind directions. All these mechanisms occur, often in tandem, during the 2 week period of interest. We simplify

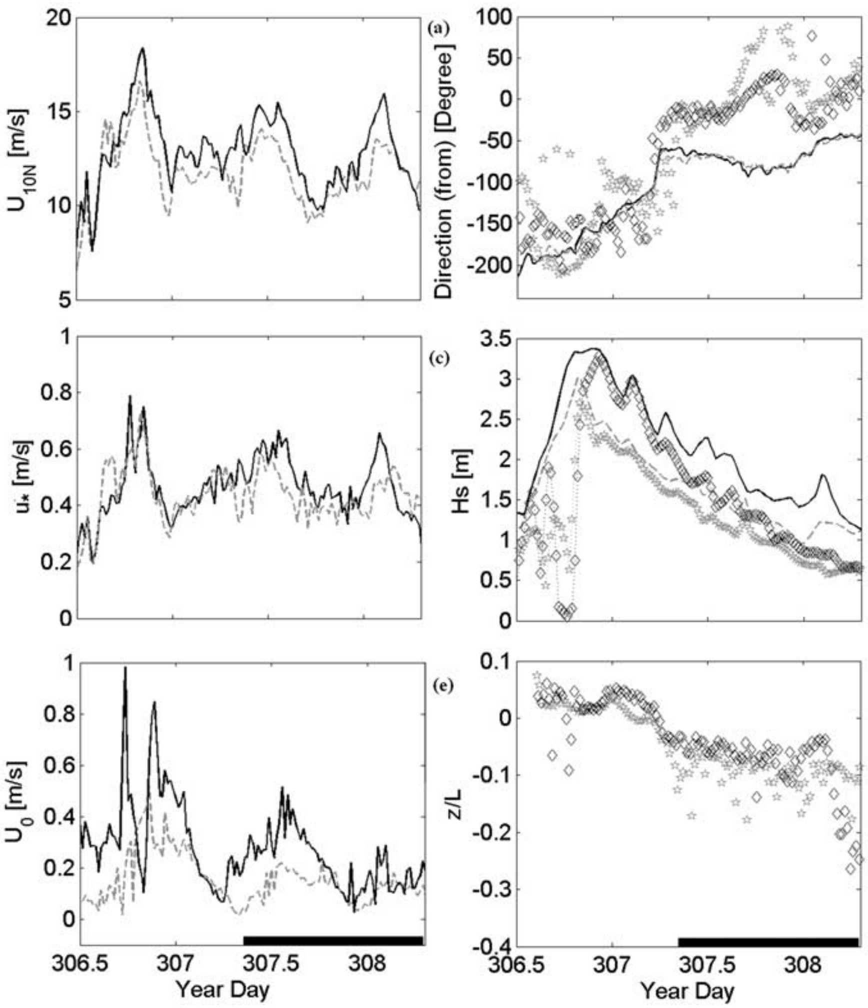

Figure 4. Data from Bravo (dashed line or star) and Yankee (solid line or diamond) buoys. (a) Wind speed; (b) wind direction (lines) and absolute current direction from OSCR (stars and diamonds); (c) friction velocity; (d) significant wave height (lines), significant height for swell (stars and diamonds); (e) surface current speed; (f) atmospheric stability. The period of interest (POI) is denoted by the black bar.

the problem by focusing on a time period with high off-wind stress angles and a single dominant mechanism. In particular, we focus on the 25 h period starting around 1400 UTC on Day 307, when relative stress angles of order 30° were seen for extended periods at both buoys. For future reference we designate this our period of interest, or POI. The rationale behind this approach can be seen in Figure 3, where we plot relative stress angle versus off-wind current component U_{cY} for the full 2-week period of Figure 1. The considerable scatter in Figure 3 can be attributed to the various effects listed above: a high correlation is expected only when currents are the dominant effect. Indeed, when other effects were absent (as during the POI, distinguished by the black dots), the stress angle was correlated with the off-wind current.

[18] The conditions during the POI are now described. On the day previous to the POI, YD 306, a cold front associated with a nearby low-pressure region passed through the area resulting in high winds (Figure 4a) and a dramatic drop in air temperature over the SHOWEX domain (not shown). Atmospheric stability (Figure 4f) remained close to neutral during most of the POI, due to the consistently high winds, becoming more unstable toward the end of the period. Prior to the passage of the front, winds were over 10 m s^{-1} from SSE, roughly shore parallel (Figure 4b), and the wavefield was near full development with H_s (significant wave height) up to 3.5 m (Figure 4d). At this point, wind, waves, currents (weak, and primarily wind forced, 0.3 m s^{-1}), and wind stress were all close to colinear (Figures 5a and 5b). As the depression passed to the north, the winds backed to the NW. During the POI, the wind was blowing against the remnant swell (Figures 5e and 5f), which decayed quickly to O(0.5 m) within 24 h, i.e., by the end of the POI. Although swell waves dominated the sea state during the POI, they are not expected to influence the stress angle, as the swell and wind were near colinear. This was clearly not the case in the hours preceding the POI, when the wind and swell were nearly perpendicular (Figures 5c and 5d). Despite this, the relative stress angle at this time was still small, possibly due to the additional effects of turning winds and surface currents. To simplify the analysis,

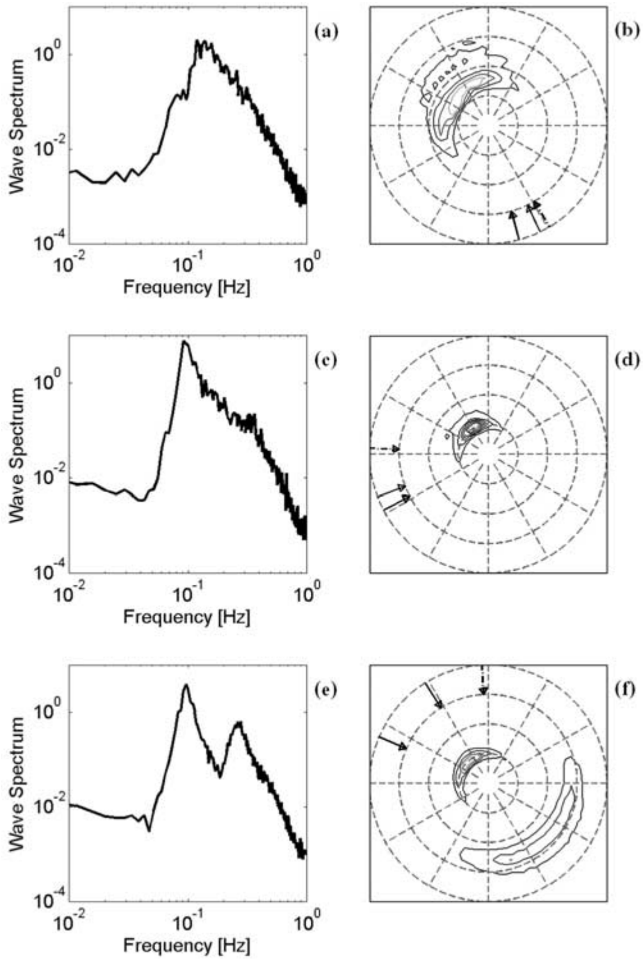

Figure 5. (left) One-dimensional and (right) two-dimensional wave spectra at Bravo. (a and b) From YD 306, 1335–1542 UTC. (c and d) From YD 307, 0204–0410. (e and f) From YD307 1125–1331. The dashed circles in the 2D spectra plots denote frequencies 0.1, 0.2, 0.3, and 0.4 Hz. North and east are at the top and right of the plots, respectively. Contours show spectral energy scaled to the maximum. The three arrows show the wind direction (black), stress direction (gray), and current direction (dashed).

the POI starts 8 h after the wind direction becomes NW, i.e., after the wind-waves reach equilibrium. The surface currents from the OSCR cells closest to Bravo and Yankee are shown in Figure 4e. Although the surface currents during the POI were typically small, there was a significant off-wind component, U_{cY} (previously plotted in Figure 3).

[19] In Figure 6, the off-wind current speed U_{cY} and the off-wind stress ($-\overline{v'w'}$) at both buoys during the POI are plotted. Four subperiods are identified, each representing a 3–5 h interval, during which the ocean currents were fairly stationary. For period A, Bravo and Yankee were located at the edge and center, respectively, of a region of strong along-coast current (Figure 7a). The NW wind passed over a region of high lateral shear before reaching Bravo; the wind stress at Bravo was steered about 30° to the current direction. Meanwhile, the wind reaching Yankee was moving over a low-shear region; the wind stress direction was only steered about 10° from mean wind direction to the current direction. During period B, there was a strong current over the whole domain (Figure 7b): the wind stress steering was similar (and large) at the two buoys.

[20] During period C, the currents throughout the domain were weak. The current speeds at and upwind of the buoys were smaller than any other time in the POI. Horizontal shears were also small. At both buoys, the wind and wind stress were aligned. See Figures 6c and 6d, which show the absolute wind, current and shear directions at the two buoys. During period D, Bravo was again immediately downwind of a region of shear (Figure 7d). Although the current speed is less than during period A, the horizontal current shear is very clear. The wind stress steering was about 30°. The other buoy, Yankee, was located in a more uniform current (Figure 7d). The horizontal current shear upwind of Yankee was weaker than at Bravo. The wind stress shifting was also less at Yankee than at Bravo.

[21] From the above, we hypothesize that horizontal shear in the upwind direction is a very important factor in influencing wind stress direction. We use the vorticity ($\omega = \frac{dU_{cY}}{dx} - \frac{dU_{cX}}{dy}$) to quantify the horizontal shear. Figures 8a–8d each present the surface current vorticity in the OSCR domain around and upwind of the buoys during one of the four periods. We pay extra attention to the vorticity in the upwind direction of Bravo and Yankee. For periods A and D, the wind-waves passed the edge of a strong along-coast current to reach Bravo. The maximum vorticity is about $1.2f$ for A and $1.1f$ for D, where f is the local Coriolis parameter. The edge of the along-coast current can be seen clearly in Figures 8a and 8d. The nonuniform current in period B has a relatively constant vorticity in the major part of the measurement area. We observe similar wind stress steering for Yankee and Bravo during period B. The vorticity during C, when currents were weak across the domain, is significantly lower than the other cases (Figure 8c). The corresponding wind stress was almost aligned with the mean wind.

[22] To further investigate the correlation between vorticity and wind stress steering for the two buoys, we average the vorticity from 10 (2×5) cells in the upwind direction (five in the upwind direction; two perpendicular to the upwind direction). The results are shown in Figure 8e for Bravo and Figure 8f for Yankee. The significant correlation between wind stress deviation with upwind current vorticity at both buoys ($\gamma^2 = 0.51$ for Bravo and $\gamma^2 = 0.45$ for Yankee) indicates that the horizontal shear has an important influence on wind stress. For periods A and D, Bravo and Yankee were just downwind of strong shear: the vorticity was high with large scatter. Period B shows high vorticity with much less scatter since the current meandering was relatively homogeneous for that time. All these periods with high upwind vorticity are with the strong wind stress steering. During period C, when the vorticity at Yankee becomes negative, the relative stress angle also changes sign.

[23] To further understand the relation between current shear and wind stress steering, we plot the off-wind current, U_{cY}, for periods A and D in Figure 9. Here $\frac{dU_{cY}}{dx}$ is the main source of vorticity during those two periods, with $\frac{dU_{cX}}{dy}$ making much less contribution but bringing significant noise to the vorticity map. From Figure 9b, Bravo and Yankee were near the maximum gradient of U_{cY} during period D. We observe a similar wind stress veering for the

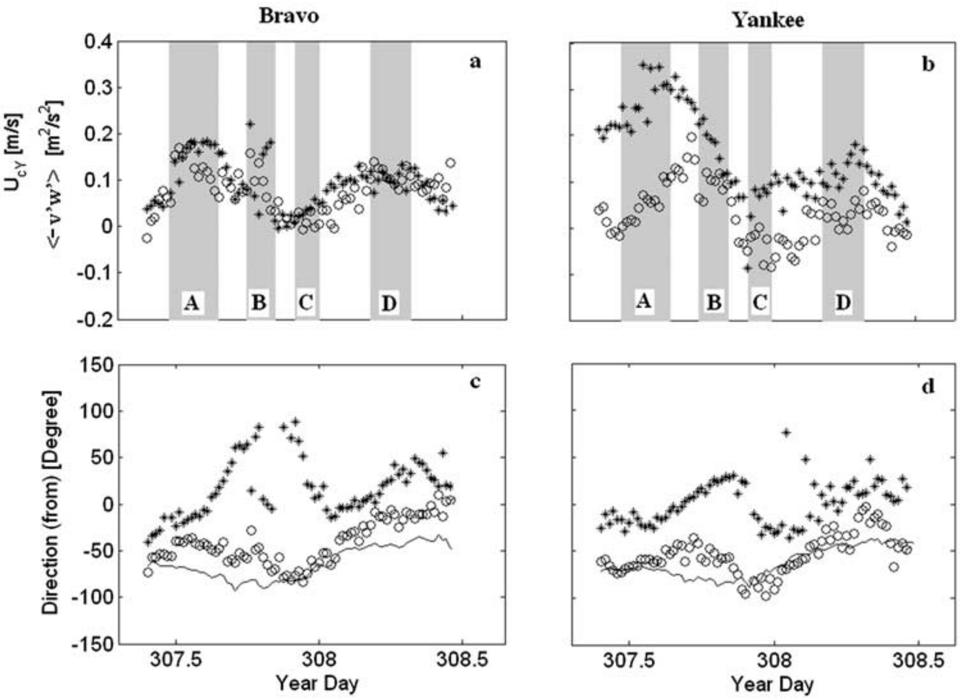

Figure 6. The off-wind current speed (asterisks) and off-wind wind stress components (circle) at (a) Bravo and (b) Yankee. A, B, C, and D are the four time periods identified in the text. Current direction (star), wind direction (solid line), and wind stress direction (circle) are also shown for (c) Bravo and (d) Yankee. Here, all directions are absolute, with 0° representing from the north.

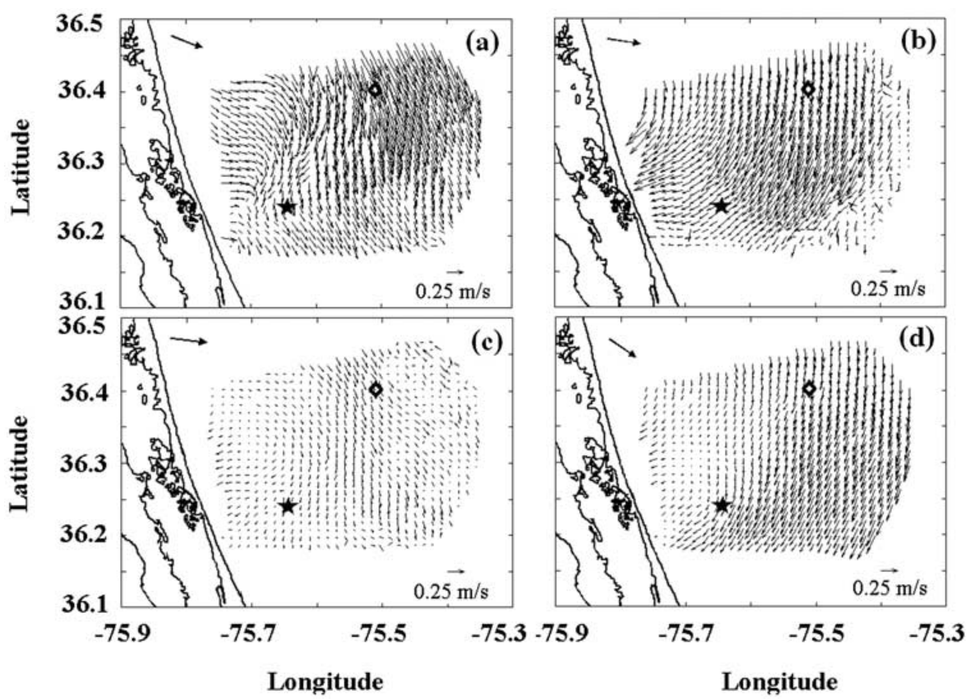

Figure 7. OSCR current vector maps for the four time periods identified in Figure 6 (a for A, etc). The two ASIS buoys Bravo (star) and Yankee (diamond) located in the scanning domain of OSCR are indicated. The arrows at the upper-left corners indicate the average wind direction. The velocity scale in the lower right refers to the current vector.

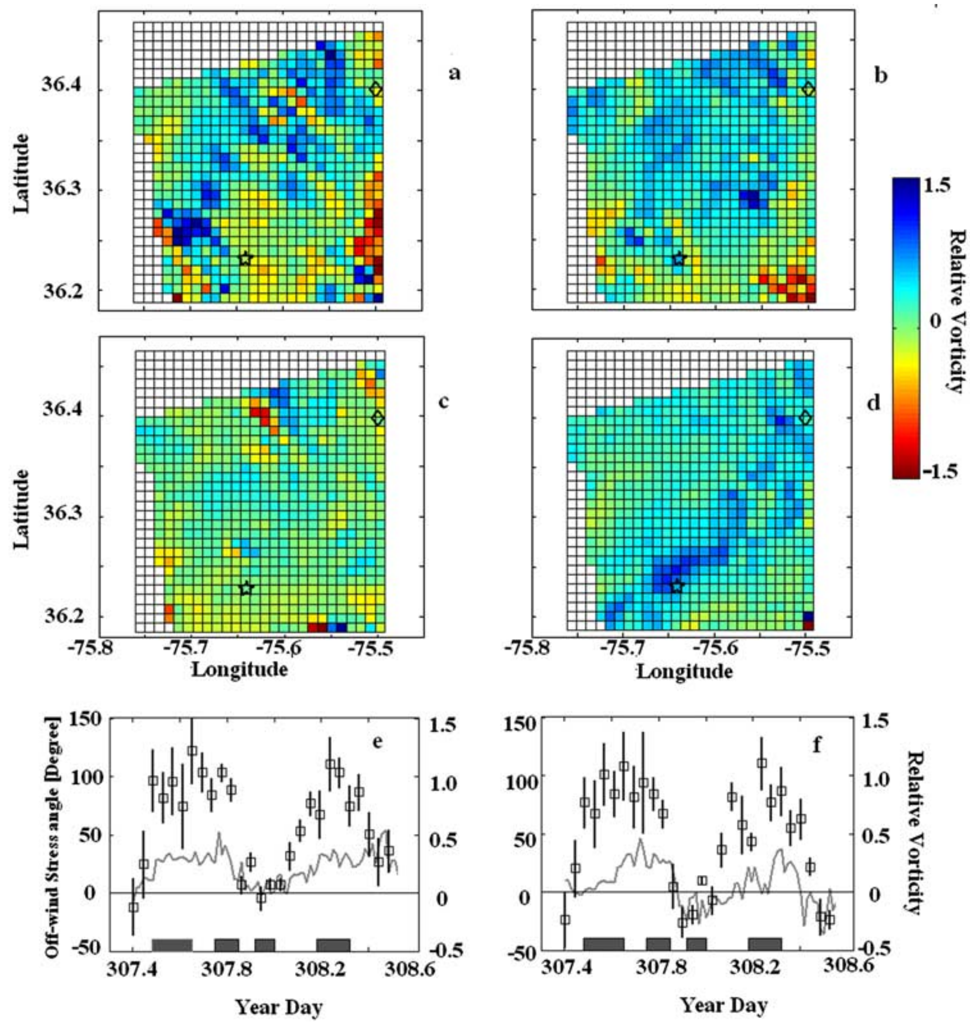

Figure 8. (a, b, c, and d) Vorticity maps for the corresponding panels in Figure 7. The ASIS buoys Bravo (star) and Yankee (diamond) are in the positions indicated. (e and f) Time series of averaged upwind relative vorticity ω/f (squares, with error bars showing one standard deviation) and off-wind stress angle (lines), where f is the local Coriolis parameter. The shaded areas at the bottom of each panel show the four periods of interest (as Figure 6).

two ASIS buoys during this period. During period A, Bravo was behind (downwind) the edge of strong current, and the wind stress direction was steered considerably from that of the wind. The situation at Yankee is similar; the horizontal shear right at Yankee in the upwind direction was not strong (Figure 9a). The differences of wind stress steering at two locations support horizontal shear as the dominant factor affecting the wind stress direction during the POI.

[24] Although current shear or vorticity appears as a dominant factor in steering the wind stress direction, the effect must be an indirect one. The wind stress is related to the roughness elements on the sea surface, which are determined by surface waves, in particular those of small scales, O(0.1 – 10 m). Hence vorticity must affect the stress through modification of the wind waves [cf. *Kenyon*, 1971; *Shay et al.*, 1996; *Haus*, 2007]. Wave information during SHOWEX is available from both OSCR and ASIS.

[25] OSCR wave directions at peak spectral frequency [*Wyatt et al.*, 2005] are shown in Figure 9a for period A. The available wave data cover a smaller area than ocean current data because the signal-to-noise requirements for processing wave height measurements are more restrictive than for currents. The peak wave directions are observed to change right after passing the strong horizontal shear (Figure 9a).

[26] The ASIS buoys provided high-resolution directional wave spectra for frequencies up to 1 Hz. The wave data set from Bravo and Yankee was used to investigate the wave refraction associated with the horizontal shear and wind stress steering. During period A, a strong current shear was just upwind of Bravo. The waves at frequencies above 0.5 Hz generally were aligned with the mean wind direction, while wind sea waves at the spectral peak (0.25 – 0.3 Hz) were shifted 30° – 40° toward the current direction (Figure 10a). The corresponding wind stress direction was steered from the mean wind direction toward the current direction. At the same time, the spectra at Yankee (Figure 11a) were almost unaffected by the horizontal shear, since it was too far from the strong along-coast current edge (Figure 7a).

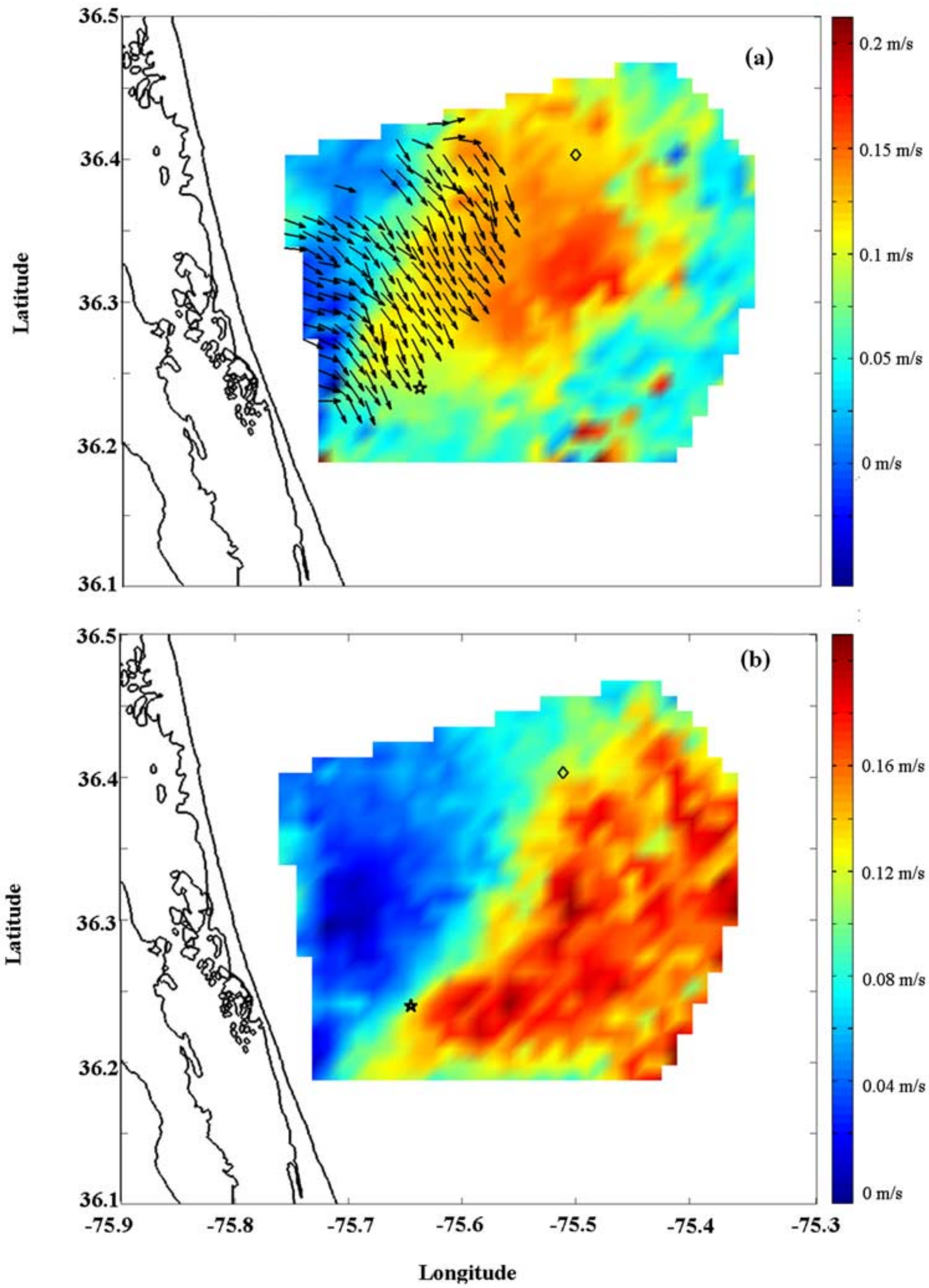

Figure 9. Off-wind current speed (U_{CY}) maps for periods (a) A and (b) D. The arrows in Figure 9a are the wind sea wave directions measured from OSCR. The star and diamond symbols show the locations of the Bravo and Yankee buoys, respectively.

[27] During period B, the current vorticity was relatively high in the entire experimental domain (Figure 8b); there was similar wave refraction for Bravo and Yankee (Figures 10b and 11b). The waves in the peak frequency bands were refracted by the high-vorticity shear associated with the curving current, but the high-frequency waves, which are under the strong wind-forcing, propagated in the same direction with the wind. The wind stress at both buoys was steered to the south by the refracted wind sea waves. The current and horizontal shear were very weak during C (Figure 7c), and the directional wind wave spectra from both buoys showed no deviation from the wind direction in any frequency band (Figures 10c and 11c). The corresponding wind stress direction was close to the mean wind direction. Period D, when the horizontal shear again became significant in the footprint of both buoys (Figure 9b), shows directional wave spectra and stress steering similar to period B (Figures 10d and 11d).

4. Discussion

[28] Our hypothesis is that the effects we are observing, namely the shifting of the wind waves and thence wind

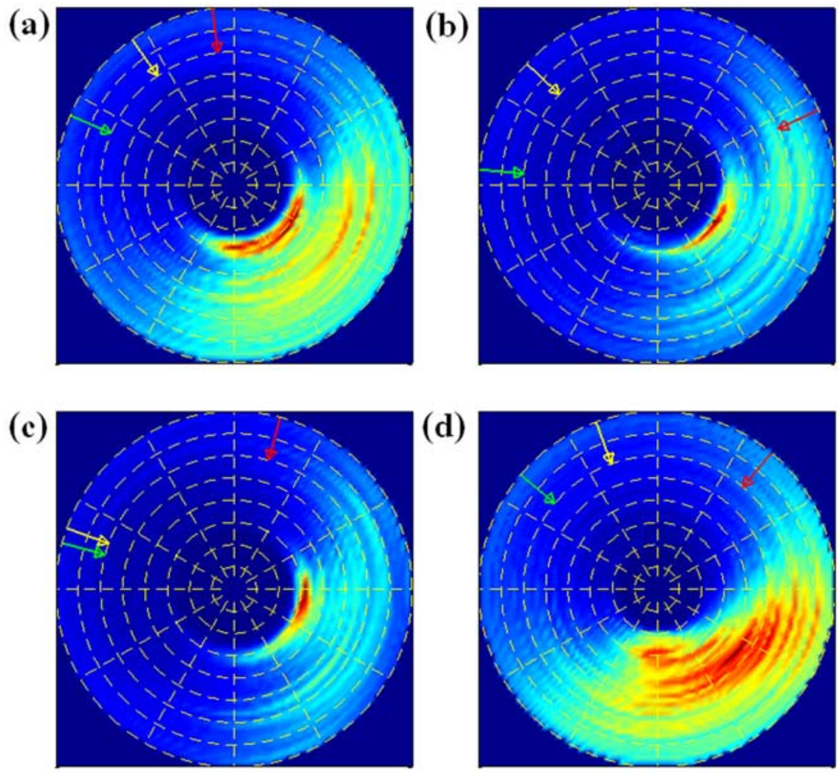

Figure 10. (a–d) The averaged directional wave spectra (times frequency squared) for Bravo at time periods A–D from Figure 6. The dashed circles represent frequency bands from 0.1 to 0.8 Hz moving outward from the center. North and east are at the top and right of each panel, respectively. The green arrow in each panel indicates the mean wind direction, the yellow arrow is the wind stress direction, and the red arrow is the current direction from OSCR at Bravo. In order to emphasize the wind sea wave peak, the wave spectra are multiplied by frequency squared.

stress away from the mean wind direction, is a result of the wind waves interacting with the surface current field. Recently, however, it was proposed that the turning of the wind waves at the SHOWEX site could be the result of the slanting fetch geometry [e.g., *Donelan et al.*, 1985; *Pettersson*, 2004] and not the currents [*Ardhuin et al.*, 2007]. Indeed, one of case studies used by *Ardhuin et al.* [2007] took place during our period A. They attribute the dominant wind-wave shifting to the slanting fetch effect and the results from the implementation of two wave models, “WAVEWATCH III” [*Tolman and Chalikov*, 1996; *Tolman*, 2002] and Coupled Rays with Eulerian Source Term [*Ardhuin and Herbers*, 2005], appear to support their conclusions, at least qualitatively. They do not include the effects of the current in either model.

[29] While slanting fetch may indeed result in a wave spectrum qualitatively similar to that observed here (i.e., a turning of the peak wind waves, but not of the wind waves in the equilibrium range), several key aspects of our observations are not consistent with the slanting fetch mechanism. First of all, Figure 9a shows a sharp gradient of the peak wave directions along the current front. The slanting fetch effect would predict gradual changes (relaxation of the peak waves back to the wind direction) with increasing fetch, with no significant change at the current front. Likewise, the slanting fetch effect cannot explain the rapid changes in relative stress angle observed at both buoys (Figures 8e and 8f). In particular, during period C, the stress angles at both buoys changed from roughly 30° away from the wind (period B) to near 0° (period C), before returning to 20° (period D). As no concurrent shifts were seen in wind speed or direction (Figure 3), the wave model of *Ardhuin et al.* [2007] would predict very similar results for those three periods. Significantly though, these stress angle changes are mirrored in the relative current vorticity changes seen in Figures 8e and 8f. Indeed, the negative vorticity at Yankee during C results in negative relative stress angles. Hence, while the slanting fetch effect may make some contribution to the observed wave spectra, the data support the hypothesis that surface currents are the key factor.

[30] We now explore the mechanisms by which currents may affect the waves and wind stress. One hypothesis is that the wind stress turning is due to refraction of the surface waves on the sheared current [*Kenyon*, 1971]. Refraction could explain the shift in the energy-containing waves away from the wind direction, but the observations show that the short waves remain in the wind direction, contrary to what is predicted by the sheared current effect.

[31] In the presence of horizontally sheared currents, wind generated waves are forced by both current shear and wind. *Alpers and Hennings* [1984] proposed a model to explain the wave patterns seen in satellite radar images.

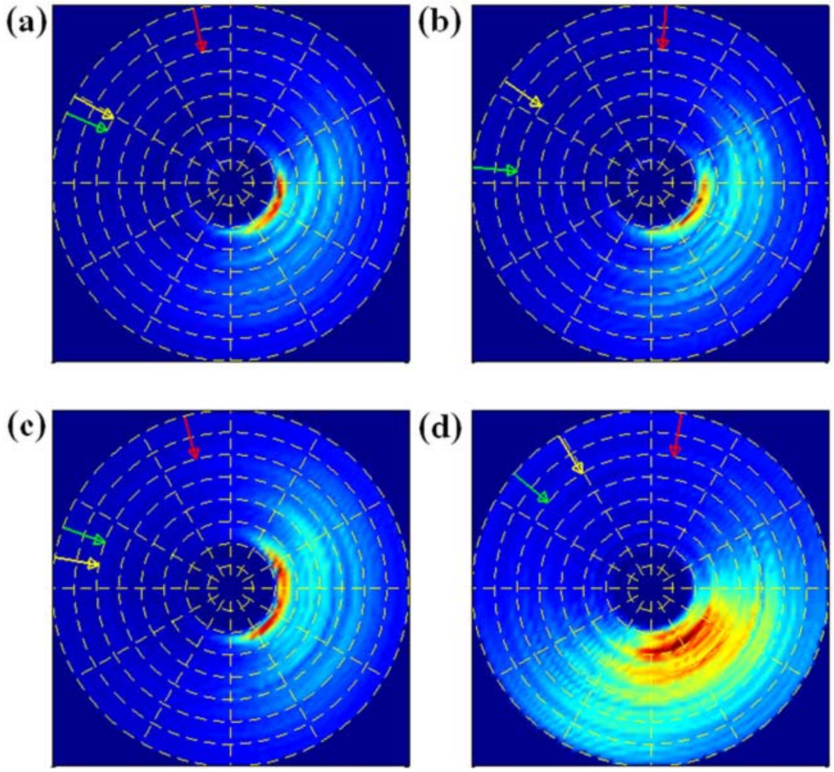

Figure 11. Similar to Figure 10, but for Yankee.

Starting from wave action conservation, and accounting for the relaxation time of surface waves, they showed that short gravity waves are prohibited from being shifted by current gradients, since the timescales of propagation across the gradient are much longer than those associated with wind forcing of the slow-moving short waves. *Kudryavtsev et al.* [2005] recently presented a new radar imaging model of oceanic current features. They confirmed the Alpers and Hennings result that short waves are not affected by current shears, and also showed that the same is not true for the longer waves near the spectral peak. Indeed, the wind-forcing time scales associated with these longer waves are much longer, so that shear current gradient is dominant. This effect is clearly seen in their Figure 7c: waves near the spectral peak are significantly shifted in direction through interaction with the current shear; for the higher-frequency equilibrium-range waves, the effect disappears. This model prediction is fully consistent with our interpretation that current shears are the key to understanding the observed changes in the wave spectrum, and thence of the stress direction.

5. Conclusion

[32] A study of current-wave-stress interaction is presented using data from the SHOWEX experiment. The near-surface currents are measured by HF radar; the wind velocity, wind stress, and high-resolution directional wave spectra are measured by instruments on two ASIS buoys moored in the radar footprint. We found that when wind was blowing across a strong surface current vorticity field, the energy-containing waves were refracted away from mean wind direction, while the equilibrium-range waves were seen to propagate in the mean wind direction with wind. The shifting of the wavefield resulted in the development of a significant off-wind stress component, the strength of which corresponded to the upwind vorticity field. These observations are consistent with recent radar imaging models which take into account the relaxation times of surface waves.

[33] Wave-current interaction remains as one of the least tested theories in the study of wave dynamics. The current-wave-stress interaction problem has only recently attracted serious attention, largely driven by the importance of such interactions in the interpretation of remote sensing products. This paper provides analysis of in situ observational data to support the idea that currents can affect wind stress through waves, which play the key role in the current-wave-stress interaction. Because of the limited data set, we cannot quantify the whole process in detail; moreover the physics governing the interaction needs to be further investigated. As has been known by sailors for millennia, wavefields can be strongly modified as they interact with strong boundary currents. As we have now shown, these changes are also fed back to the atmosphere through modifications to the surface stress. These changes are known to cause errors in present scatterometer model functions. It is important to consider that the whole process mentioned above is not a one-way process (*current* → *wave* → *wind stress*) but one which involves a complex interaction such as (*current* ↔ *wave* ↔ *wind stress* ↔ *current*). Further research along these lines will lead to an improved understanding of the complicated

processes of wave-current-stress interaction and to improved scattering models for remote sensing.

[34] **Acknowledgments.** We gratefully acknowledge support from ONR for the SHOWEX departmental research initiative (N00014-97-1-0348, N00014-03-1-0230, and N00014-99-1-1092). FZ and WD were further supported by NSF-OCE-0220459 and BH by NSF-OCE-0526491. This work could not have been carried out without the support of a large number of technicians, staff, and scientists. In particular we acknowledge the efforts of Steve Cavendish, Joe Gabriele, Jorge Martinez, Mike Rebozo, the officers and crew of the R/V *Oceanus*, and the staff of the USACE Field Research Facility at Duck, North Carolina. We also thank Lucy Wyatt for her processing of the OSCR wave data.

References

Alpers, W., and I. Hennings (1984), A theory of the imaging mechanism of underwater bottom topography by real and synthetic aperture radar, *J. Geophys. Res.*, *89*, 10,529–10,546, doi:10.1029/JC089iC06p10529.

Anctil, F., M. A. Donelan, W. M. Drennan, and H. C. Graber (1994), Eddy correlation measurements of air-sea fluxes from a Discus buoy, *J. Atmos. Oceanic Technol.*, *11*, 1144–1150, doi:10.1175/1520-0426(1994)011<1144:ECMOAS>2.0.CO;2.

Ardhuin, F., and T. H. C. Herbers (2005), Numerical and physical diffusion: Can wave prediction models resolve directional spread?, *J. Atmos. Oceanic Technol.*, *22*, 886–892, doi:10.1175/JTECH1723.1.

Ardhuin, F., T. H. C. Herbers, G. P. van Vledder, K. P. Watts, R. Jensen, and H. C. Graber (2007), Swell and slanting-fetch effects on wind wave growth, *J. Phys. Oceanogr.*, *37*, 908–931, doi:10.1175/JPO3039.1.

Busch, N. E. (1977), Fluxes in the surface boundary layer over the sea, in *Modeling and Prediction of the Upper Layers of the Ocean*, edited by E. B. Kraus, pp. 72–91, Pergamon, Oxford, U.K.

Capon, J. (1969), High-resolution frequency-wavenumber spectrum analysis, *Proc. IEEE*, *57*, 1408–1418, doi:10.1109/PROC.1969.7278.

Cornillon, P., and K.-A. Park (2001), Warm core ring velocities inferred from NSCAT, *Geophys. Res. Lett.*, *28*, 575–578, doi:10.1029/2000GL011487.

Dickinson, S., K. A. Kelly, M. J. Caruso, and M. J. McPhaden (2001), A note on comparisons between the TAO and NASA scatterometer wind vectors, *J. Atmos. Oceanic Technol.*, *18*, 799–806, doi:10.1175/1520-0426(2001)018<0799:CBTTBA>2.0.CO;2.

Donelan, M. A. (1990), Air-sea interaction, in *The Sea: Ocean Engineering Science 9*, edited by B. LeMéhauté and D. Hanes, pp. 239–292, John Wiley, New York.

Donelan, M. A., J. Hamilton, and W. H. Hui (1985), Directional Spectra of wind generated waves, *Philos. Trans. R. Soc. London, Ser. A*, *315*, 509–562, doi:10.1098/rsta.1985.0054.

Drennan, W. M., and L. K. Shay (2006), On the variability of the fluxes of momentum and sensible heat, *Boundary Layer Meteorol.*, *119*, 81–107, doi:10.1007/s10546-005-9010-z.

Drennan, W. M., M. A. Donelan, N. Madsen, K. B. Katsaros, E. A. Terray, and C. N. Flagg (1994), Directional wave spectra from a Swath ship at sea, *J. Atmos. Oceanic Technol.*, *11*, 1109–1116, doi:10.1175/1520-0426(1994)011<1109:DWSFAS>2.0.CO;2.

Drennan, W. M., H. C. Graber, D. Hauser, and C. Quentin (2003), On the wave age dependence of wind stress over pure wind seas, *J. Geophys. Res.*, *108*(C3), 8062, doi:10.1029/2000JC000715.

Geernaert, G. L., F. Hansen, M. Courtney, and T. Herbers (1993), Directional attributes of the ocean surface wind stress vector, *J. Geophys. Res.*, *98*, 16,571–16,582, doi:10.1029/93JC01439.

Graber, H. C., B. K. Haus, L. K. Shay, and R. D. Chapman (1997), HF radar comparisons with moored estimates of current speed and direction: Expected differences and implications, *J. Geophys. Res.*, *102*, 18,749–18,766, doi:10.1029/97JC01190.

Graber, H. C., E. A. Terray, M. A. Donelan, W. M. Drennan, J. Van Leer, and D. B. Peters (2000), ASIS–A new air-sea interaction spar buoy: Design and performance at sea, *J. Atmos. Oceanic Technol.*, *17*, 708–720, doi:10.1175/1520-0426(2000)017<0708:AANASI>2.0.CO;2.

Grachev, A. A., C. W. Fairall, J. E. Hare, J. B. Edson, and S. D. Miller (2003), Wind stress vector over ocean waves, *J. Phys. Oceanogr.*, *33*, 2408–2429, doi:10.1175/1520-0485(2003)033<2408:WSVOOW>2.0.CO;2.

Haus, B. K. (2007), Surface current effects on the fetch-limited growth of wave energy, *J. Geophys. Res.*, *112*, C03003, doi:10.1029/2006JC003924.

Haus, B. K., H. C. Graber, L. K. Shay, and T. M. Cook (2004), Alongshelf variability of a coastal buoyancy current during the relaxation of downwelling favorable winds, *J. Coastal Res.*, *19*, 409–420.

Kaimal, J. C., and J. E. Gaynor (1991), Another look at sonic anemometry, *Boundary Layer Meteorol.*, *56*, 401–410, doi:10.1007/BF00119215.

Kelly, K. A., S. Dickinson, M. J. McPhaden, and G. C. Johnson (2001), Ocean currents evident in satellite wind data, *Geophys. Res. Lett.*, *28*, 2469–2472, doi:10.1029/2000GL012610.

Kelly, K. A., S. Dickinson, and G. C. Johnson (2005), Comparisons of scatterometer and TAO winds reveal time-varying surface currents for the tropical Pacific Ocean, *J. Atmos. Oceanic Technol.*, *22*, 735–745, doi:10.1175/JTECH1738.1.

Kenyon, K. E. (1971), Wave refraction in ocean currents, *Deep Sea Res.*, *18*, 1023–1034.

Kitaigorodskii, S. A. (1973), *The Physics of Air–Sea Interactions*, 237 pp., Isr. Program for Sci. Transl., Jerusalem.

Kudryavtsev, V., D. Akimov, J. Johannessen, G. Caudal, and B. Chapron (2005), On radar imaging of current features: 1. Model and comparison with observation, *J. Geophys. Res.*, *110*, C07016, doi:10.1029/2004JC002505.

Large, W. G., and S. Pond (1981), Open ocean momentum flux measurements in moderate to strong winds, *J. Phys. Oceanogr.*, *11*, 324–336, doi:10.1175/1520-0485(1981)011<0324:OOMFMI>2.0.CO;2.

Monin, A. S., and A. M. Obukhov (1954), Basic laws of turbulent mixing in the ground layer of the atmosphere, *Akad. Nauk. SSSR Geofiz. Inst. Tr.*, *151*, 163–187.

Pettersson, H. (2004), Wave growth in a narrow bay, 33 pp., Ph.D. dissertation, Univ. of Helsinki, Finland.

Pettersson, H., H. C. Graber, D. Hauser, C. Quentin, K. K. Kahma, W. M. Drennan, and M. A. Donelan (2003), Directional wave measurements from three wave sensors during the FETCH experiment, *J. Geophys. Res.*, *108*(C3), 8061, doi:10.1029/2001JC001164.

Polito, P., J. P. Ryan, W. T. Liu, and F. P. Chavez (2001), Oceanic and atmospheric anomalies of tropical instability waves, *Geophys. Res. Lett.*, *28*, 2233–2236, doi:10.1029/2000GL012400.

Prandle, D. (1987), The fine-structure of nearshore tidal and residual circulation revealed by HF radar surface current measurements, *J. Phys. Oceanogr.*, *17*, 231–245, doi:10.1175/1520-0485(1987)017<0231:TFSONT>2.0.CO;2.

Rennie, S. E., J. L. Largier, and S. J. Lentz (1999), Observations of a pulsed buoyancy current downstream of Chesapeake Bay, *J. Geophys. Res.*, *104*, 18,227–18,280, doi:10.1029/1999JC900153.

Richardson, P. L., and T. K. McKee (1984), Average seasonal variation of the Atlantic equatorial currents from historical ship drifts, *J. Phys. Oceanogr.*, *14*, 1226–1238, doi:10.1175/1520-0485(1984)014<1226:ASVOTA>2.0.CO;2.

Rieder, K. F., J. A. Smith, and R. A. Weller (1994), Observed directional characteristics of the wind, wind stress and surface waves on the open ocean, *J. Geophys. Res.*, *99*, 22,589–22,596, doi:10.1029/94JC02215.

Shay, L. K., P. C. Zhang, H. C. Graber, and E. J. Walsh (1996), Simulated surface wave current interactions during SWADE, *Global Atmos. Ocean Syst.*, *5*, 125–150.

Smith, S. D. (1980), Wind stress and heat flux over the ocean in gale force winds, *J. Phys. Oceanogr.*, *10*, 709–726, doi:10.1175/1520-0485(1980)010<0709:WSAHFO>2.0.CO;2.

Stewart, R. H., and J. W. Joy (1974), HF radar measurement of surface current, *Deep Sea Res.*, *21*, 1039–1049.

Tolman, H. L. (2002), User manual and system documentation of WAVEWATCH-III version 222, *Tech. Rep. 222*, 133 pp., NOAA, Silver Spring, Md.

Tolman, H. L., and D. Chalikov (1996), Source terms in a third-generation wind wave model, *J. Phys. Oceanogr.*, *26*, 2497–2518, doi:10.1175/1520-0485(1996)026<2497:STIATG>2.0.CO;2.

Weisberg, R. H. (1984), Seasonal adjustment in the equatorial Atlantic during 1983 as seen by surface moorings, *Geophys. Res. Lett.*, *11*, 733–735, doi:10.1029/GL011i008p00733.

Wu, J. (1975), Wind-induced drift currents, *J. Fluid Mech.*, *68*, 49–70, doi:10.1017/S0022112075000687.

Wyatt, L. R., G. Liakhovetski, H. C. Graber, and B. Haus (2005), Factors affecting the accuracy of SHOWEX HF radar wave measurements, *J. Atmos. Oceanic Technol.*, *22*, 847–859, doi:10.1175/JTECH1728.1.

Zemba, J., and C. A. Friehe (1987), The marine atmospheric boundary layer jet in the Coastal Ocean Dynamics Experiment, *J. Geophys. Res.*, *92*, 1489–1496, doi:10.1029/JC092iC02p01489.

W. M. Drennan, H. C. Graber, B. K. Haus, and F. W. Zhang, Rosenstiel School for Marine and Atmospheric Science, University of Miami, Miami, FL 33149, USA. (wdrennan@rsmas.miami.edu)